

Measuring the integrated Sachs-Wolfe effect from the low-density regions of the universe

Fuyu Dong,^{1,2,4} Yu Yu,^{1,2} Jun Zhang,^{1,2}[★] Xiaohu Yang,^{1,2,3} Pengjie Zhang,^{1,2,3}[†]

¹*Department of Astronomy, School of Physics and Astronomy, Shanghai Jiao Tong University, Shanghai, 200240, China*

²*Shanghai Key Laboratory for Particle Physics and Cosmology, Shanghai, 200240, China*

³*Division of Astronomy and Astrophysics, Tsung-Dao Lee Institute, Shanghai Jiao Tong University, Shanghai, 200240, China*

⁴*School of Physics, Korea Institute for Advanced Study (KIAS), 85 Hoegiro, Dongdaemun-gu, Seoul, 02455, Republic of Korea*

Accepted XXX. Received YYY; in original form ZZZ

ABSTRACT

The integrated Sachs-Wolfe (ISW) effect is caused by the decay of cosmological gravitational potential, and is therefore a unique probe of dark energy. However, its robust detection is still problematic. Various tensions between different data sets, different large scale structure (LSS) tracers, and between data and the Λ CDM theory prediction, exist. We propose a novel method of ISW measurement by cross correlating CMB and the LSS traced by “low-density-position” (LDP, Dong et al. (2019)). It isolates the ISW effect generated by low-density regions of the universe, but insensitive to selection effects associated with voids. We apply it to the DR8 galaxy catalogue of the DESI Legacy imaging surveys, and obtain the LDPs at $z \leq 0.6$ over ~ 20000 deg² sky coverage. We then cross correlate with the Planck temperature map, and detect the ISW effect at 3.2σ . We further compare the measurement with numerical simulations of the concordance Λ CDM cosmology, and find the ISW amplitude parameter $A_{\text{ISW}} = 1.14 \pm 0.38$ when we adopt a LDP definition radius $R_s = 3'$, fully consistent with the prediction of the standard Λ CDM cosmology ($A_{\text{ISW}} = 1$). This agreement with Λ CDM cosmology holds for all the galaxy samples and R_s that we have investigated. Furthermore, the S/N is comparable to that of galaxy ISW measurement. These results demonstrate the LDP method as a competitive alternative to existing ISW measurement methods, and provide independent checks to existing tensions.

Key words: Cosmology: Integrated Sachs-Wolfe Effect – Cosmology: large-scale structure of universe – Cosmology: dark energy

1 INTRODUCTION

The integrated Sachs-Wolfe (ISW) effect (Sachs & Wolfe 1967) probes the time variation of gravitational potential, through the induced CMB temperature fluctuation

$$\Delta T(\hat{n}) = \frac{2}{c^3} T_0 \int \dot{\Phi}(\mathbf{r}, \hat{n}) \, d\mathbf{r} . \quad (1)$$

Here \hat{n} is the line of sight, T_0 the mean temperature of CMB, c the speed of light, $\dot{\Phi}$ the time derivative of the gravitational potential along, a the cosmic scale factor and r the comoving radial distance. The gravitational potential Φ at large/linear scale is time independent, if gravity is GR, the universe is flat and the total matter density $\Omega_m = 1$. Observations of primary CMB (Planck Collaboration et al. 2016a) show that our universe is flat. Then within the framework of general relativity, any detection of the ISW effect

would serve as a smoking gun of dark energy. It can then be used to constrain the dark energy equation of state, and even clustering of dark energy around horizon scale (e.g. Weller & Lewis (2003); Bean & Doré (2004); Hu & Scranton (2004); Cabré et al. (2006); Mota et al. (2008); de Putter et al. (2010)). Alternatively, it can be used to test GR at cosmological scales (Hu 2003; Zhang 2006; Giannantonio et al. 2006; Cabré et al. 2007; Fang et al. 2008; Giannantonio et al. 2012), constrain primordial non-Gaussianities (Nadathur et al. 2012), or probe GR backreaction (Rácz et al. 2017).

The major factor limiting the cosmological application of ISW is its weak signal, overwhelmed by the primary CMB. It can be separated from primary CMB, by cross-correlating with the large scale structure (LSS) (Crittenden & Turok 1996; Seljak & Zaldarriaga 2000). However, to further suppress the cosmic variance, CMB surveys of nearly full sky coverage and wide and deep galaxy surveys are both required. From the release of the first year WMAP data, there

[★] betajzhang@sjtu.edu.cn

[†] zhangpj@sjtu.edu.cn

have been various works to measure the ISW effect (Fosalba et al. 2003; Boughn & Crittenden 2004; Afshordi 2004; Afshordi et al. 2004; Fosalba & Gaztañaga 2004; Nolta et al. 2004; Boughn & Crittenden 2005; Padmanabhan et al. 2005; Corasaniti et al. 2005; Vielva et al. 2006; McEwen et al. 2006; Cabré et al. 2007; Rassat et al. 2007; Raccanelli et al. 2008; Hernández-Monteagudo 2010; Massardi et al. 2010; Schiavon et al. 2012; Giannantonio et al. 2012; Planck Collaboration et al. 2014; Shajib & Wright 2016; Planck Collaboration et al. 2016b). The analyzed CMB experiments include both WMAP and Planck. The analyzed galaxy surveys include SDSS, NVSS, 2MASS, WISE, etc. The LSS tracers include SDSS main galaxies and luminous red galaxies in optical bands, radio galaxies, AGNs, and even weak gravitational lensing reconstructed from CMB (Planck Collaboration et al. 2016b). Although some claimed detection significances ($\sim 2-4\sigma$) may be questionable (Giannantonio et al. 2012; Hernández-Monteagudo et al. 2014), these measurements are in general consistent with the Λ CDM prediction.

Besides directly using galaxies as LSS tracers, entities derived with galaxy surveys such as superclusters and voids are also explored to measure the ISW effect (Granett et al. 2008; Pápai et al. 2011; Planck Collaboration et al. 2014). These measurements have different S/N and different systematics, and therefore are highly complementary to ISW measurements with galaxies. For example, ISW measured from voids may have less contamination from radio emission associated with galaxies. However, there are tensions between existing measurements and between measurements and theoretical prediction. For example, Granett et al. (2008) stacked the most significant 50 clusters/voids (superclusters/supervoids) identified with SDSS photo- z data, and found a 4σ detection of the ISW effect. However, after investigated by other papers, this detection has been found difficult to explain (Hunt & Sarkar 2010; Inoue et al. 2010; Ilić et al. 2014; Hotchkiss et al. 2015; Kovács & Granett 2015).

Tensions persists in later measurements with different void catalogues. In most cases excess signals are reported compared to the Λ CDM prediction (Nadathur et al. 2012). For example, Cai et al. (2014) found that their detection with SDSS voids is at odds with simulations of a Λ CDM universe at $\sim 2\sigma$. In term of the ISW amplitude A_{ISW} ($A_{\text{ISW}} = 1$ in the standard Λ CDM cosmology), Kovács (2018) found with BOSS supervoids $A_{\text{ISW}} \approx 9$. Kovács et al. (2019) found with DES super-voids $A_{\text{ISW}} \approx 4.1$.

These tensions are unlikely caused by new physics beyond Λ CDM, since the ISW measurements with galaxies in the same surveys/cosmic volumes are usually consistent with the Λ CDM prediction. Furthermore, it is found that the ISW measurements with voids rely heavily on the void catalogues (e.g. Granett et al. (2008); Kovács & Granett (2015)) and therefore the associated systematics, if uncorrected. In addition, null detections were also reported in observations and favored in simulations (Hotchkiss et al. 2015; Ilić et al. 2014).

Among all possibilities leading to the above controversies, void identification in observations likely plays a major role. Voids are defined as low number density regions in the galaxy distribution field. But in low density regions, the galaxy number distribution suffers from relatively larger shot noise. This makes the identification of voids and their centers/radii difficult. The low number density further am-

plifies the impact of non-uniform galaxy (radial and angular) selection function in spectroscopic redshift surveys, and making its correction more challenging than the case of galaxy clustering. Situation becomes even worse for the photometric data, for which the smearing effect of redshift errors of galaxies in the line-of-sight will “merge” voids. These issues also complicate the correspondence between voids in observations and in simulations/theory, and make the theoretical interpretation difficult.

Taking these issues into account, in this paper we revisit the measurement of ISW effect by considering a new LSS tracer – “low-density-position” (LDP) (Dong et al. 2019). LDPs are the collection of sky positions, after removing positions within a given radius of any observed galaxy. Statistically speaking, they correspond to low density regions. The density threshold depends on the radius to perform the cut and the mean number density of observed galaxies. So by varying the cut radius, LDPs can also serve as intermediate case between galaxies and voids. So they will provide independent check on the above tensions found between voids and the concordance Λ CDM, and between observations of voids and galaxies. Furthermore, comparing to voids, LDPs are more straightforward to identify in both observations and in simulations, making the data interpretation more reliable. In Dong et al. (2019), we have used LDPs to achieve significant detection of weak lensing using CFHTLenS data, and to differentiate dark energy models. In this work, we treat LDPs as density tracers and focus on the LDP-temperature correlation measurement. Our aim is to provide independent ISW measurement, which is then used to test the concordance Λ CDM cosmology, and cross-check with existing ISW measurements with voids.

The paper is organized as follows: In §2, we introduce the data sets and procedures to measure the LDP-temperature correlations ($\omega_{T\ell}$). In §3, we calculate the theoretical prediction from mocks generated by a Λ CDM N-body simulation. §4 shows our main results of ISW measurement with the LDP method. In §5, we give conclusion and discussions about related issues. Some further technical details are presented in the appendix, along with the measured CMB-galaxy correlation (appendix C).

2 OPERATING WITH THE OBSERVATIONAL DATA

We choose the DR8 galaxy catalogue of the DESI imaging surveys to construct the LDP field, and then cross with Planck SMICA map to measure the ISW effect in the low-density regions of the universe.

2.1 Galaxy Catalogue and LDP generation

The DR8 galaxy catalogue¹ is a combination of four surveys: BASS (Zou et al. 2019), MzLS (Silva et al. 2016), DECaLS (The Dark Energy Survey Collaboration 2005; Blum

¹ http://batc.bao.ac.cn/~zouhu/doku.php?id=projects:desi_photoz;

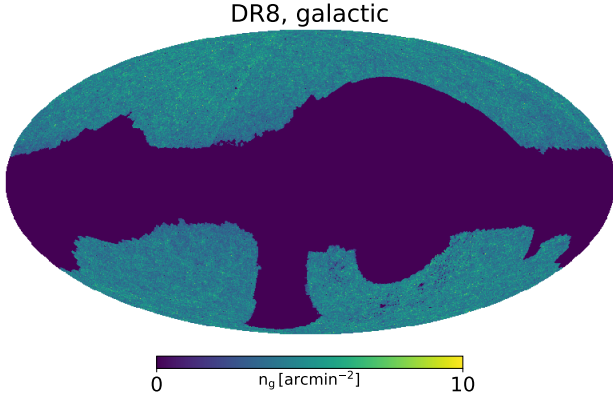


Figure 1. Source distribution in the DR8 catalogue of the BASS + MzLS + DECaLS + DES imaging surveys. The depth of color represents the number of galaxies per arcmin².

et al. 2016) and DES (Abbott et al. 2018). They are independent optical imaging surveys with close photometric systems. The first three together with the infrared WISE survey (Wright et al. 2010) aim at providing galaxy and quasar targets for the follow-up Dark Energy Spectroscopic Instrument survey (DESI; DESI Collaboration et al. (2016)). In the DR8 data release, BASS+MzLS locates in the north Galactic cap, DES locates in the south Galactic cap, and DECaLS locates in both north and south Galactic caps along the equator, resulting in a joint sky coverage $\sim 20000 \text{ deg}^2$. The galaxy catalogue provides the photometrically estimated redshifts (hereafter photo- z), apparent magnitudes in g, r, z bands and stellar masses of galaxies. It is the largest galaxy data set currently available. Its large sky coverage is useful to reduce the statistical errors in our measurements, a key to improve the ISW measurement.

The galaxy catalogue includes those sources which have detections in g, r and z bands, and $r < 23$. Furthermore, stars have been excluded through star-galaxy classification. As we can see from Fig.1, the surface density of galaxies is reasonably uniform across the sky. The residual non-uniformity (inhomogeneous selection function) is a severe issue for measuring the galaxy auto-correlation. But it is less an issue for cross-correlation measurements presented here, since the selection function is largely uncorrelated with the LSS and its impact on ISW-galaxy cross correlation is taken into account in the random catalogue and in the simulation mocks. Coordinates of galaxies have been converted from equatorial coordinate system into galactic coordinate system, in which all the operations are done in the rest of the paper.

2.1.1 LDP identification

We identify LDPs and define the associated LSS field through the following procedures:

- *Generating Survey Masks.* Sets of uniformly distributed random catalogues are provided in the DR8 website². Each

² <http://legacysurvey.org/dr8/files/#random-catalogs>

$z_m = 0.3, \text{Mag}_c - 5\text{lgh} = -21, R_s = 3 \text{ arcmin}$

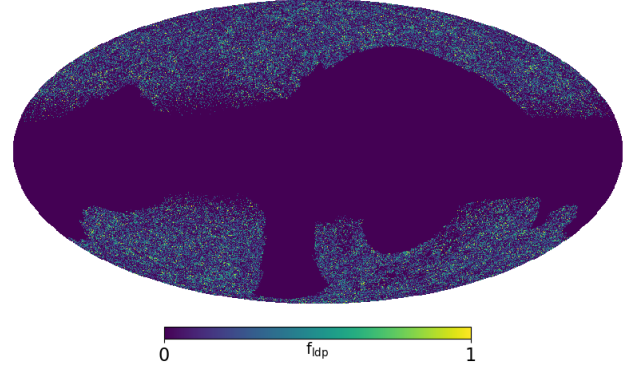


Figure 2. The full-sky f_{ldp} (the fraction of low-density points in each cell/pixel) distribution. LDPs are generated with cut radius $R_s = 3'$, for the galaxy sample with magnitude cut $\text{Mag}_c - 5\text{lgh} = -21$ and photo- z cut $0.2 < z < 0.4$.

random point contains the exposure times for g, r, z bands based upon the sky coordinate drawn independently from the observed distribution. We choose random points whose exposure times in all three bands are greater than zero and MASKBITS³ equals to zero to produce the survey masks which populate the same sky coverage and geometry with the galaxy catalogue.

- *Generating LDPs.* LDPs depend on the galaxy sample, so we need to first select the galaxy sample for LDP generation. (1) First, we calculate the r -band absolute magnitudes of galaxies with their apparent magnitudes and photo- z .⁴ (2) Then similar to the approach in Dong et al. (2019), we select galaxies brighter than a certain absolute magnitude, and within a photo- z band $[z_m - 0.1, z_m + 0.1]$ to form the galaxy sample for LDP generation. $\Delta z = 0.2$ is chosen as the photo- z error dispersion $\lesssim 0.1$ on average. (3) Within this galaxy sample, we circle around each galaxy with an angular radius R_s , and remove all positions within this radius from the sky. The remaining regions are defined as LDPs candidates. We also remove the LDP candidates lying within the masks. There are no galaxies within radius R_s to any given LDPs, otherwise these points will be excluded by the LDP definition procedure. The underlying density in this region, with \bar{N} galaxy on the average over the survey volume but $N = 0$ galaxy for the selected LDPs, has a PDF $P(\delta|N=0) \propto \exp(-\bar{N}(1+\delta))P(\delta)$. $P(\delta)$ peaks at $\delta_{\text{peak}} < 0$. $P(\delta|N=0)$ then peaks at $\delta < \delta_{\text{peak}} < 0$. Therefore indeed LDPs occupy under-dense regions. (4) We put LDPs on uniform grids generated with HEALPix (Górski et al. 2005).

³ MASKBITS greater than zero means that the source at this position overlaps with bad or saturated pixels, like bright star mask, globular cluster and so on.

⁴ The absolute magnitudes used have not been K-corrected. Since galaxies within the same photo- z bin have similar K-correction and the LDP generation is only sensitive to relative brightness between these galaxies, this lack of K-correction is not an issue for our purpose.

[!htp]

Table 1. The galaxy samples we use in the DR8 catalogue.

z_m	$\text{Mag}_c - 5\text{lgh}$	$n_{\text{gal}} (10^6)$				R_s [arcmin]	\bar{f}_{ldp}				$\delta_{\text{l,max}}$			
		-20.5	-21	-21.5	-22		-20.5	-21	-21.5	-22	-20.5	-21	-21.5	-22
0.1	0.1	1.73	0.81	0.28	-	3	0.55	0.75	0.9	-	0.81	0.34	0.11	-
						5	0.22	0.47	0.75	-	3.44	1.13	0.33	-
0.3	0.3	-	4.53	1.31	0.26	3	-	0.22	0.62	0.9	-	3.56	0.62	0.11
						5	-	0.02	0.28	0.75	-	42.7	2.51	0.32
0.5	0.5	-	-	1.66	0.24	3	-	-	0.55	0.91	-	-	0.83	0.1
						5	-	-	0.21	0.77	-	-	3.86	0.3

' n_{gal} ' is the number of galaxies in each galaxy sample.

' \bar{f}_{ldp} ' is the average value of f_{ldp} .

$\delta_{\text{l,max}}$ is the maximum δ_{l} .

Although the finer the grids, the more accurate the LDP distribution can be obtained, we adopt $N_{\text{side}} = 4096$ HEALPIX resolution due to the limitation of the number of random points.

2.1.2 The LDP over-density maps

Different LDPs correspond to different under-dense regions. For a given LDP, the distance to the nearest galaxy R_{min} satisfies $R_{\text{min}} \geq R_s$. Statistically speaking, the larger the R_{min} , the more negative the underlying matter overdensity δ_m . Therefore to improve the S/N of ISW-LDP measurement, we need to put larger weight for LDPs with larger R_{min} . Theoretically speaking there exists an optimal mapping between R_{min} and δ_m , and we should find and use that relation to figure out the optimal weighting. We leave this issue for further investigation. Here we take a suboptimal, nevertheless workable, weighting scheme.

We smooth the LDPs with coarse grids, and define the LDP over-density field in each cell as:

$$\delta_{\text{l}} = \frac{f_{\text{ldp}} - \bar{f}_{\text{ldp}}}{\bar{f}_{\text{ldp}}}, \quad (2)$$

Here we divide the whole sky into lower resolution cells with $N_{\text{side}} = 512$ (comparing to $N_{\text{side}} = 4096$ previously). The corresponding cell size is $6.87'$. f_{ldp} is the area proportion of LDPs occupying the given cell. It equals the number of LDPs in each cell divided by n_{grid} . n_{grid} is the number of fine grids within the coarse cell, which equals 64 here. The maximum δ_{l} occurs for those cells completely occupied by LDPs, corresponding to regions with the most negative δ_m . In order to reduce the impact of survey mask and edge effect on our calculation, we make a selection on the cells being used. We require that the random points which do not satisfy the criteria in §2.1.1 should take up less than $\eta = 30\%$ of the area of cells. Otherwise, the cells will be disregarded. Smaller η results into less cells used for the measurement and therefore larger statistical errors. Larger η results into larger misidentification of low-density regions and therefore weaker ISW signal. The adopted $\eta = 30\%$ is a balance between the two. As tested in simulation, with this ratio the magnitude of our measured LDP-ISW signal being depressed is less than 4% compared to the one without mask effect. In observation, we also find that this way of cell-selection helps to enhance the amplitude of ω_{T1}^0 .

In this procedure, the fewer galaxies are selected, the

more LDPs would be produced, and vice versa. Taking this into consideration, we control the size of galaxy samples so that their distribution is neither too crowded nor too sparse, otherwise the δ_{LDP} generation will lack of accuracy in statistics. For $z_m = 0.1$, we consider setting $\text{Mag}_c - 5\text{lgh}$ respectively to be -20.5, -21 and -21.5. For $z_m = 0.3$, $\text{Mag}_c - 5\text{lgh}$ is set to -21, -21.5 and -22. For $z_m = 0.5$, $\text{Mag}_c - 5\text{lgh}$ is set to -21.5 and -22. Galaxies with redshift less than 0.01 are not used due to their too high number density. In Table 1 we introduce these galaxy samples and LDPs generated with them. Fig.2 shows one example of the f_{ldp} distribution, for which LDPs are generated with parameters $z_m = 0.3$, $\text{Mag}_c - 5\text{lgh} = -21$ and $R_s = 3'$.

2.2 CMB Data

We use the Planck SMICA map for the ISW-LDP measurement. The SMICA map has removed secondary CMB anisotropies such as the thermal Sunyaev Zel'dovich effect, which is also correlated with LSS. It also removes galactic foregrounds, which may be correlated with the galaxy mask/selection and therefore may bias the cross correlation measurement. We downgrade the map from $N_{\text{side}} = 2048$ to $N_{\text{side}} = 512$ resolution and adopt WMAP 9-year CMB mask (Hinshaw et al. 2013; Kovács et al. 2019) to mask out pixels contaminated by Galactic dust or known point sources. We find that this resolution downgrading only influences the cross-correlation signals at angular separations less than 10 arcmin, as we would expect from the large scale origin of the ISW effect.

3 PREDICTING THE ISW EFFECTS WITH A N-BODY SIMULATION

Although implementing the LDP analysis is straightforward at the data side, it is highly non-trivial at the theory side due to complicated relation between LDPs and the underlying density/potential field. This is further complicated by various selection effect in observations. Therefore we will use a N-body simulation to generate ISW maps. The same simulation is used to generate mock galaxy catalogues and LDPs, under given observational conditions. They are then used to predict the ISW-LDP correlation signal.

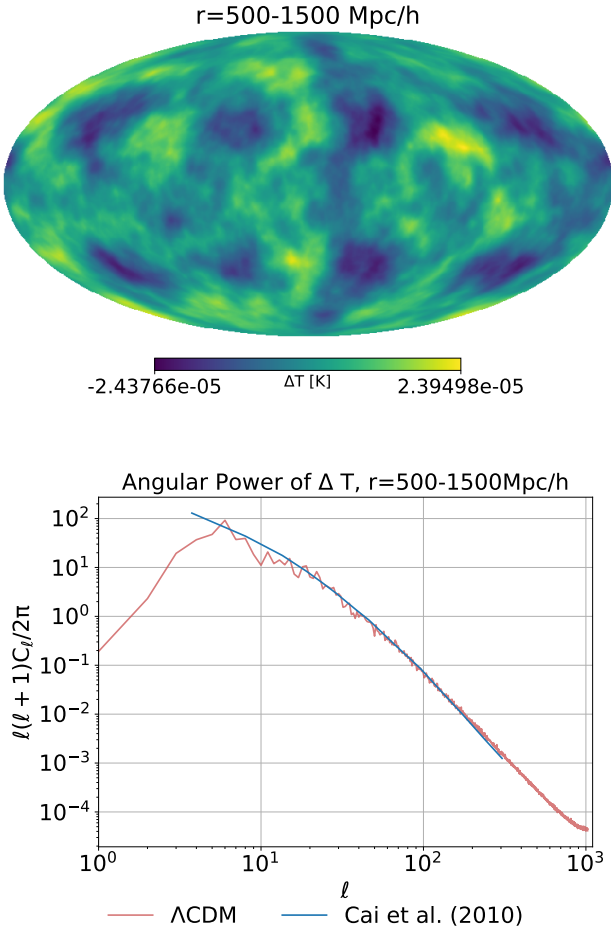


Figure 3. The ISW induced ΔT generated using our simulation. The upper panel shows the full-sky temperature fluctuation map, for which the ray-tracing is done between the radial distance [500, 1500] Mpc/h. While in the lower panel we show its corresponding power spectrum. The blue line shows the prediction from Cai et al. (2010) based on the linear theory, and the red curve is our result. They are well consistent.

3.1 N-body Simulation

The ISW signal is mostly contributed from the large scale mode, so here we use the 1200Mpc/h N-body simulation from the CosmicGrowth simulation series (Jing 2019). It contains 3072^3 simulation particles, and adopts the flat Λ CDM cosmology, with $\Omega_c = 0.223$, $\Omega_b = 0.0445$, $\Omega_\Lambda = 0.732$, $\sigma_8 = 0.83$, $h=0.71$, and $n_s = 0.968$. Halos are identified with FoF group finder, and subhalos are identified with HBT (Han et al. 2012).

3.2 Construction of Full Sky ISW Map

As shown in Eq. 1, the ISW induced ΔT is an integration of $\dot{\Phi}$ along the line-of-sight. Making use of the Poisson equation⁵, we obtain $\dot{\Phi}$ in Fourier space:

$$\dot{\Phi}(\vec{k}, t) = \frac{3}{2} \left(\frac{H_0}{k} \right)^2 \Omega_m \left[\frac{\dot{\delta}(\vec{k}, t)}{a^2} - \frac{\delta(\vec{k}, t)}{a} \right]. \quad (4)$$

Here $\rho(t)$ is the matter density, $\bar{\rho}(t)$ the mean density, δ the over-density ($\delta \equiv (\rho - \bar{\rho})/\bar{\rho}$), H_0 the current Hubble parameter and Ω_m the present value of matter density parameter. In the linear regime, $\dot{\delta}(\vec{k}, t) = \dot{D}(t)\delta(\vec{k}, z=0)$, where $D(t)$ is the linear growth factor. For our purpose, it is sufficient to neglect the nonlinear evolution (Rees-Sciama effect). Therefore $\dot{\Phi}(\vec{k}, t) \propto k^{-2}(1 - \beta(t))H\delta(\vec{k}, t)/a$, where $\beta(t) \equiv d \ln D(t)/d \ln a$.

In simulation, we construct the Φ field in the following way. Firstly, we assign dark matter particles into 3D grids under Cartesian coordinate, and construct the density field $\delta(\vec{x})$. During this process, we use a grid of 512^3 cells for our simulation box. Then we perform the Fast Fourier Transform on the density field to compute its Fourier form $\delta(\vec{k})$. It is then used to yield the $\dot{\Phi}(\vec{k}, t)$ field in Fourier space. At last, we perform the inverse Fourier transform to obtain $\dot{\Phi}(\vec{x})$ in real space. Above procedures are repeated for eight output snapshots at redshift 0, 0.058, 0.151, 0.253, 0.364, 0.485, 0.616 and 0.76. To avoid the discontinuities of Φ at boundaries, we assume periodic boundary conditions when using our simulation to construct $\Phi(\vec{x})$ on a cube whose size length is larger than 1200 Mpc/h.

Next, we choose the center of spliced cube as the location of observer, and generate angular evenly distributed rays from it using HEALPix with $N_{\text{side}} = 512$ resolution. For each ray, we accumulate the temperature fluctuations along its line of sight using Eq. (1) by taking fixed discrete steps. Note that, values of $\dot{\Phi}$ for the same grid generated from different snapshots are different. So for each step, according to its position on the ray we find out the snapshot at that lookback time, and assign it the value of $\dot{\Phi}$ of its nearest grid. In this way, we are able to construct full sky maps of the ISW effect using the density field.

In this paper we construct the ISW induced $\Delta T(\hat{n})$ with a maximum redshift 0.7. However, there will be two problems arising from the periodic boundary conditions assumed in the above when constructing the $\Delta T(\hat{n})$ map. The first problem is that light rays will pass through the same structure every certain distance, leading to larger fluctuations along these directions. This distance is the shortest for light rays along the main axis of the simulation box, equaling to 1200 Mpc/h. The second problem is that the same structure is seen in multi-directions. As pointed out in Cai et al. (2010) that the first issue can be solved by generating maps with the radial depth less than the simulation boxsize. The second issue does not matter as long as the angular scales of our analysis are less than the angular size subtended by the simulation box.

In the top panel of Fig. 3 we show the predicted ΔT

$$\Phi(\vec{k}, t) = -\frac{3}{2} \left(\frac{H_0}{k} \right)^2 \Omega_m \frac{\delta(\vec{k}, t)}{a}, \quad (3)$$

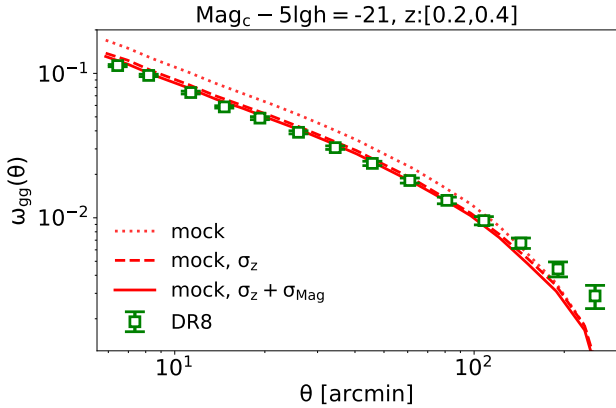


Figure 4. The auto correlation for galaxies brighter than -21 at $z_m = 0.3$. The green data points show the measurement in observation, with jackknife error bars. The red solid line is the result for mock galaxies when both σ_{Mag} and σ_z are introduced. The red dashed line is the result for mock galaxies when only σ_z is introduced. The red dotted line is the result when neither σ_{Mag} nor σ_z is considered.

map generated by integrating along the line-of-sight of the observer for the range $500 < r_c < 1500$ Mpc/h, and in the bottom panel we show its power spectrum (red solid line). The blue solid line is the linear theoretical prediction from Cai et al. (2010), which has assumed a very similar cosmology to us. These two lines are found in good consistency.

3.3 Generating LDPs with Mock Galaxies

Similar to the operation in Dong et al. (2019), we draw correspondence between galaxies and halos/subhalos by matching the galaxy-subhalo abundance (SHAM). With absolute magnitudes of galaxies computed in §2.1, we measure the luminosity functions for three redshift bins: [0.01,0.2], [0.2,0.4] and [0.4,0.6]. Then for each used snapshot, we compare the number of halos/subhalos with mass at the accretion time greater than M to the number of galaxies with luminosity less than L at that redshift. Subhalos from different snapshots are used to fulfill the corresponding radial distance slices. And we adopt the mask of DR8 in simulation in order to ensure the same angular selection of galaxies as in observation.

To better mimic the real situation, we also add scatters to the redshifts and luminosities of mock galaxies. Firstly, with the probability distribution function of redshift dispersion $P(\sigma_z, z)$ measured in observation⁶, we randomly generate σ_z for each galaxy. Then for the purposes of this paper we take the assumption that $p(z_{\text{photo}}|z)$ follows a Gaussian function with a zero mean and a scatter σ_z . We randomly move the positions of galaxies in redshift space and update the absolute magnitudes of mock galaxies according to $z - z_{\text{photo}}$. Thirdly, we introduce a constant scatter $\sigma_{\text{Mag}} = 0.375$ dex to the absolute magnitude to mimic the

galaxy-halo/subhalo relation (Yang et al. 2008). After introducing these uncertainties, we redo the SHAM to ensure the same luminosity function of mock galaxies as in observation. In this way, we generate the mock photo- z catalogue for $z < 0.6$ in simulation. We don't consider for the redshift bin [0.6,0.8] as the generation of its volume-limited mock galaxy sample may suffer from the incompleteness of galaxies at higher redshifts when σ_z is introduced.

To validate our galaxy mocks, we compare the angular distribution of our mock galaxies to observation in Fig.4 for $z_m = 0.3$. For this purpose, the two-point correlation-function at angular separation θ is calculated in the simple way of:

$$\omega_{gg}(\theta) \equiv \langle \delta_g(\hat{n}_1) \delta_g(\hat{n}_2) \rangle. \quad (5)$$

where $\hat{n}_i \cdot \hat{n}_j = \cos\theta$ and δ_g is the number over-density of galaxies. δ_g is obtained as:

$$\delta_g(\hat{n}) = \frac{n_g(\hat{n}) - \bar{n}_g}{\bar{n}_g}, \quad (6)$$

where n_g is the number density of galaxies in the HEALPix cell with $N_{\text{side}} = 512$ resolution. The absolute magnitudes of these galaxies are less than -21, and their redshifts are within the slice [0.2, 0.4]. It shows that the ω_{gg} of mock galaxies is consistent with it in observation. Adding magnitude uncertainty will slightly suppress the correlation function. Adding redshift uncertainty influences the correlation function more significantly. We also find that the brighter the galaxy, the larger the impact. In §5 we will discuss its influence on our LDP-ISW signal measurement.

Notice that the auto-correlation function estimator above is by no means optimal and by no means bias-free, comparing to the standard Landy-Szalay estimator. It is only used for the purpose of comparing the mock and data. Since we use the same estimator for both the mock and the data, the consistency in ω_{gg} shows that our galaxy mocks well represent the observed galaxy distribution. Since this paper does not focus on the auto-correlation analysis, this comparison is sufficient for current purpose.

Then we repeat the operations described in §2.1 to generate LDPs in simulation. Fig.5 shows the cross correlations of LDP overdensity δ_l with the matter density δ_m . The tight correlation confirms our expectation that δ_l is indeed a good tracer of LSS. Furthermore, the cross correlation-function has the opposite sign to the matter auto-correlation function or the matter-galaxy cross-correlation function. This confirms that δ_l is a good tracer of low-density regions of the universe.

4 ISW-LDP CROSS CORRELATION MEASUREMENTS

With the data analysis tools and simulation tools presented in previous sections, we now proceed to the LDP-ISW cross correlation measurements and their theoretical interpretation.

4.1 The cross-correlation measurements

We adopt a simple estimator for the angular correlation-function $\omega_{T\ell}(\theta)$ between the CMB temperature map and the

⁶ Considering our galaxy sample, for $z_m = 0.1, 0.3$ and 0.5 , we only use galaxies whose absolute magnitudes are respectively lower than -20, -20.5 and -21 to get $P(\sigma_z, z)$.

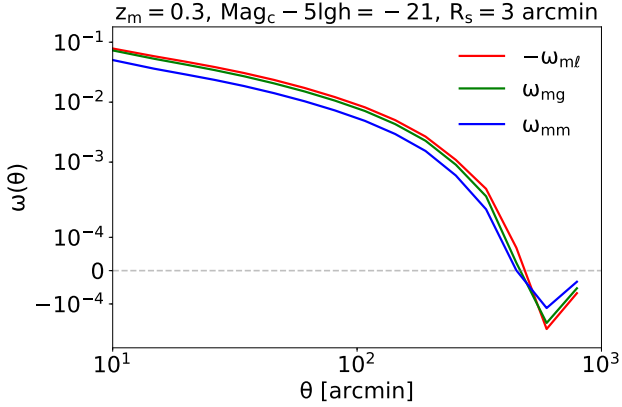


Figure 5. The cross-correlation between the LDP-matter (red line), galaxy-matter (green line) and matter-matter correlation functions, in our mock. The similarity in shapes of the three correlations and the significance of the ω_{ml} signal show that the LDP field is indeed tightly correlated with the matter distribution. The negative sign in ω_{ml} shows that the LDP field indeed probes under-dense regions.

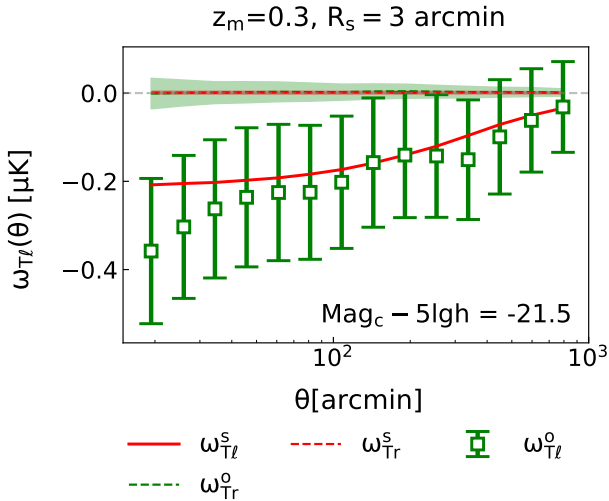


Figure 6. The LDP-CMB cross correlation measured for $z_m = 0.3$. LDPs are generated with galaxies whose absolute magnitudes are less than -21.5 and $R_s = 3'$. The green square points show $\omega_{T\ell}^o$ from observation and the red solid line is the prediction from simulation. The green and red dashed lines show results of the null test (ω_{Tr}) respectively for observation and simulation. They are calculated by correlating randomly disturbed δ_1 with ΔT . Error bars shown for $\omega_{T\ell}^o$ are estimated with the CMB rotating strategy. The green (red) shadow area shows one σ range of ω_{Tr}^o (ω_{Tr}^s).

LDP over-density δ_1 map,

$$\omega_{T\ell}(\theta) = \langle \delta_T(\hat{n}_1) \delta_\ell(\hat{n}_2) \rangle, \quad (7)$$

and we evaluate it with TreeCorr package (Jarvis 2015). $\delta_T(\hat{n}) = T(\hat{n}) - T_0$ is the temperature fluctuation, and δ_ℓ the LDP overdensity. With the data in both observation and simulation, we have 4 cross-correlation measurements. $\omega_{T\ell}^o$ is calculated with DR8 galaxy catalogue. ω_{Tr}^o is obtained by randomly shuffling δ_1 in different cells and correlated with

ΔT . And this operation is repeated for 100 times to obtain the average value and variance. Here the superscript ‘‘o’’ denotes observation. ω_{Tr}^o is useful for the null-test and, if non-zero, should be subtracted from $\omega_{T\ell}^o$ to correct the mean impact of various selection effects such as the survey geometry, mask and mean CMB fluctuations. Namely, the finally estimated ISW-LDP cross correlation is

$$\hat{\omega}_{T\ell}(\theta) = \omega_{T\ell}^o(\theta) - \omega_{Tr}^o(\theta). \quad (8)$$

Correspondingly, $\omega_{T\ell}^s$ and ω_{Tr}^s are calculated with mock catalogue in simulation.

Fig.6 shows one of such measurements, in which the LDPs are generated with parameters $\text{Mag}_c - 5lgh = -21.5$, $R_s = 3$ arcmin and $z_m = 0.3$. The first finding is that $\omega_{Tr}^o \approx 0$. The scatter is $\sim 2 \times 10^{-3} \mu\text{K}$, about 10 percent of $\omega_{T\ell}^o$. Therefore it does not matter whether ω_{Tr}^o is subtracted or not. ω_{Tr}^s is also consistent with zero ($1 \times 10^{-3} \mu\text{K}$), with much smaller σ as no CMB components/foregrounds are considered in our simulation. The second finding is that, the measured cross correlation is in good agreement with the theoretical prediction $\omega_{T\ell}^s$.⁷ We repeat the above calculations for three redshift bins: $z_m = 0.1, 0.3, 0.5$, and for different choices of critical magnitude. Fig.7 & 8 show the results of $R_s = 5'$ and $3'$ respectively. In general we find good agreement between observation and theory/simulation.

4.2 The covariance estimation and the detection significance

Error bars shown in Fig.6 are directly estimated from the CMB map by rotating it around different axis with angle $\Delta\Phi$. This is based on the consideration that the ISW induced temperature fluctuation is much smaller than the fluctuation from the original CMB. The rotation strategy has been proposed in Sawangwit et al. (2010), in which the WMAP maps have been rotated around the galactic pole to identify galactic contamination. However, any choice of axis is feasible, since one does not expect correlations for a large rotation angle $\Delta\Phi$. So scatters from independent rotations should reflect the intrinsic variance in the measurements, including the instrumental effect. To perform independent measurements, a minimum rotation $\Delta\Phi = 30^\circ$ is required, as suggested in Giannantonio et al. (2012). Therefore, each rotation axis leaves 11 independent samples of cross-correlation measurement. We choose 18 positions on CMB map as the rotation axis⁸, with angular distances between them no less

⁷ When given the prediction of $\omega_{T\ell}^s$ from simulation, there is one issue that needs further attention. Considering that photo-z errors are added to our mock galaxies, there will be galaxies from other redshifts entering the redshift bin $[z_m - 0.1, z_m + 0.1]$ used for generating LDPs. So the ISW induced temperature fluctuations from the neighboring redshifts will associate with $\delta_1(z_m)$. In this case, it is better to generate $\delta_T(\hat{n})$ by integrating temperature fluctuations within a broader redshift range. However, to avoid the enlarged $\Delta T(\hat{n})$ problem caused by the repeated structures discussed in §3.2, we choose to generate the full-sky map using the ϕ field within $[z_m - 0.2, z_m + 0.2]$. The redshift depth 0.4 is considered both from the fact that $\bar{\sigma}_z \sim 0.1$ and the boxsize of simulation.

⁸ We make the following sets of (θ, ϕ) as rotation axis: $\theta = [90^\circ, 120^\circ, 150^\circ, 180^\circ, 210^\circ, 240^\circ, 270^\circ, 300^\circ, 330^\circ]$, $\phi = [30^\circ, 60^\circ]$.

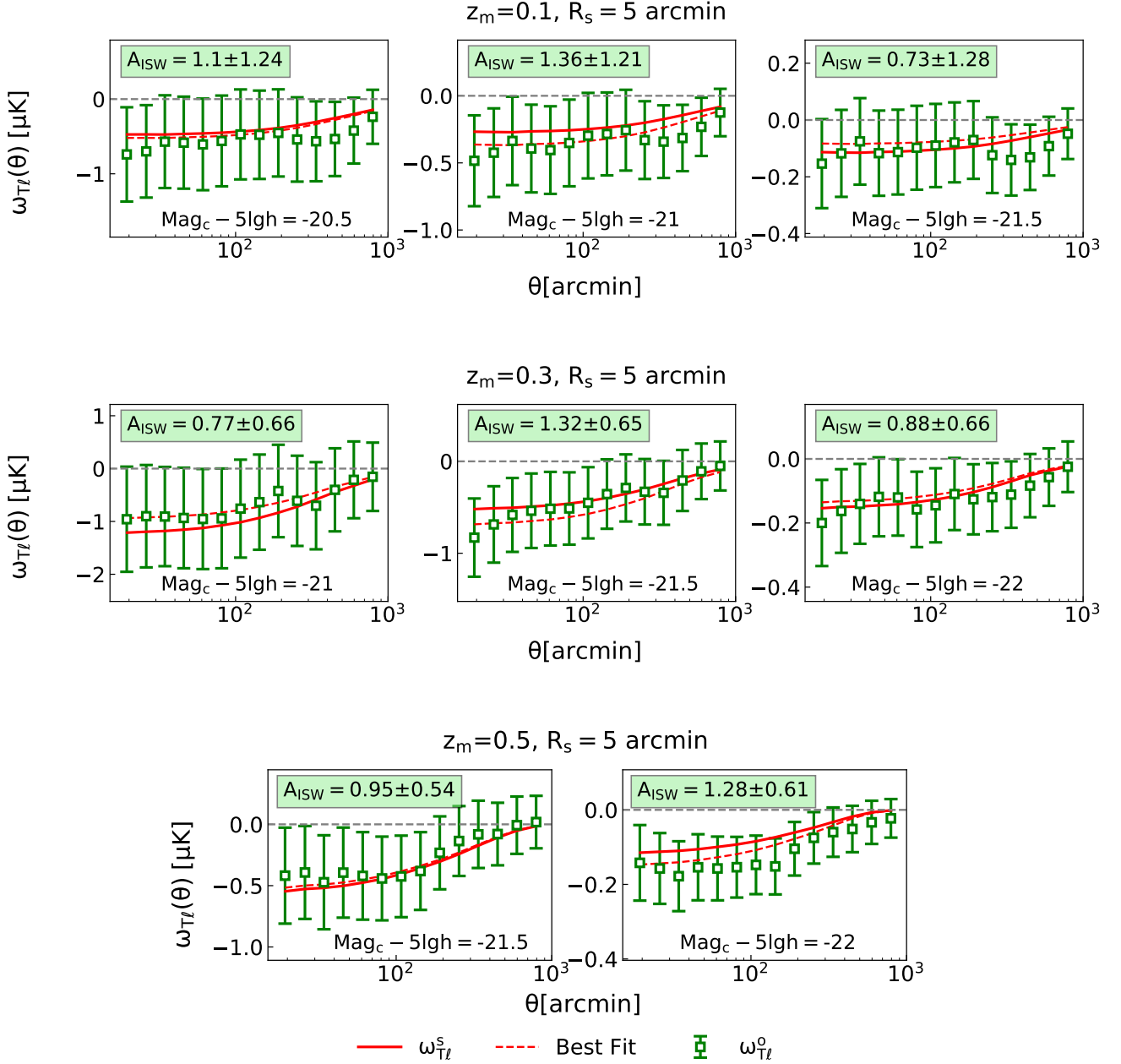


Figure 7. The LDP-CMB cross correlation measured for three redshifts: $z_m = 0.1, 0.3$ and 0.5 . R_s is set to 5 arcmin . For redshift $z_m = 0.1$, the left, middle, and right columns are for $\text{Mag}_c - 5lgh = -21.5, -21, -20.5$ respectively. For $z_m = 0.3$, the three columns are for $\text{Mag}_c - 5lgh = -22, -21.5$ and -21 . And for $z_m = 0.5$, the two columns are for $\text{Mag}_c - 5lgh = -22$ and -21.5 .

than 30° . In this way, we get 198 independent measurements of $\omega_{T\ell}$. The covariance matrix is estimated by

$$C_{ij} = \frac{1}{N} \sum_{n=1}^N [(\omega_{T\ell,n}(\theta_i) - \bar{\omega}_{T\ell}(\theta_i)) \times (\omega_{T\ell,n}(\theta_j) - \bar{\omega}_{T\ell}(\theta_j))]. \quad (9)$$

We show the normalized covariance matrix $C_{ij}/\sqrt{C_{ii}C_{jj}}$ for $\omega_{T\ell}^0$ in the lower panel of Fig.9. It indicates strong correlations between different angular scales, which is a common feature for correlation-function measurement. $\sigma_\omega = C_{ii}^{1/2}$ is the error bar shown in Fig.6, for each angular bin θ_i .

For each galaxy/LDP sample, the total S/N of the ob-

servational signal can be calculated as

$$\frac{S}{N} = \left[\sum_{i,j} \omega_{T\ell}^0(\theta_i) C_{ij}^{-1} \omega_{T\ell}^0(\theta_j) \right]^{1/2}. \quad (10)$$

The results are shown in Table 2. LDP samples of different photo- z bins are uncorrelated, so the total S/N of the ISW measurement of all three photo- z bins ($\alpha = 1, 2, 3$) is

$$(S/N)_t = \sqrt{\sum_{\alpha=1}^3 (S/N)_\alpha^2}. \quad (11)$$

Depending on the choice of LDP samples, the total S/N

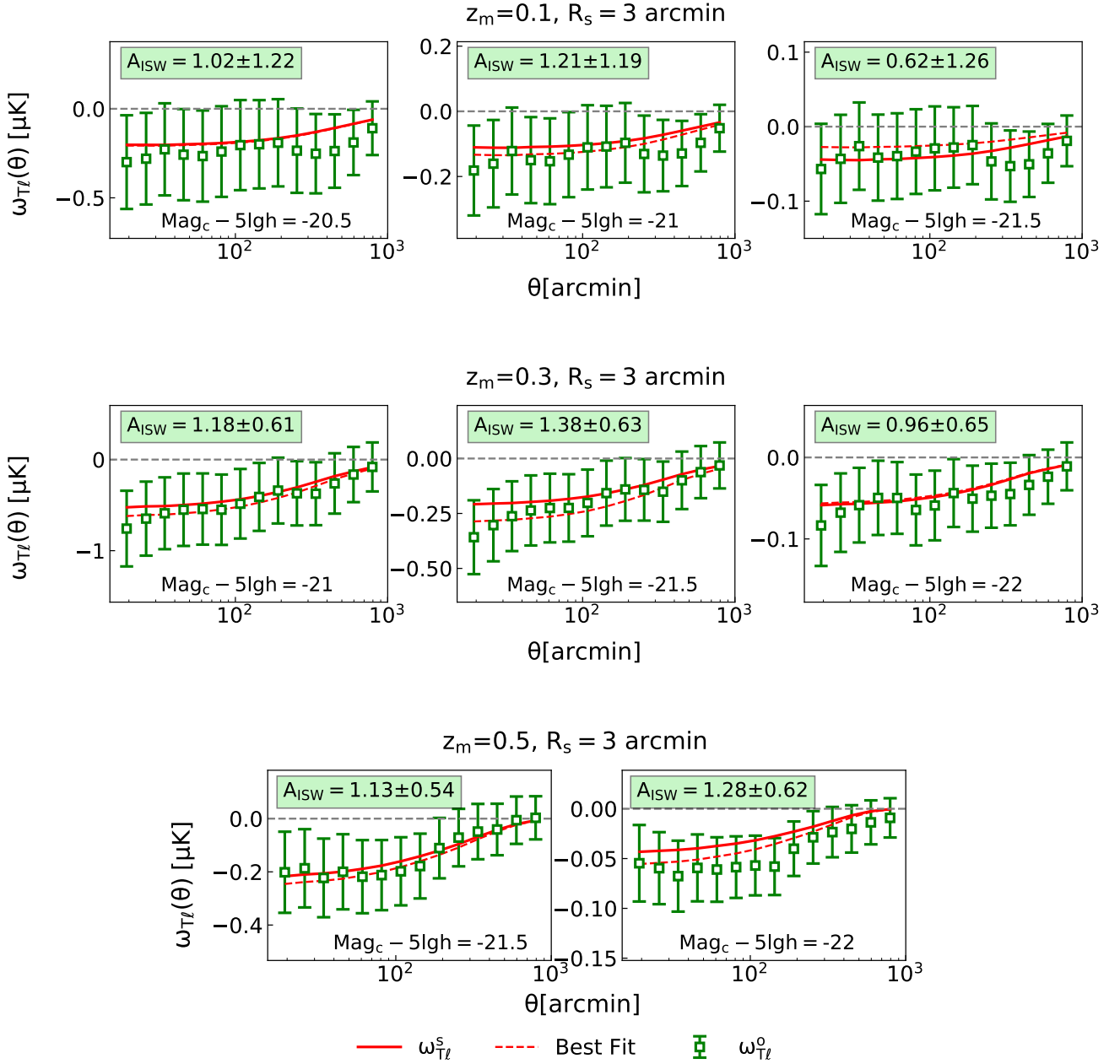


Figure 8. Similar to Fig.7, but with R_s shrunk to 3 arcmin.

of three photo- z bins varies. For example, when $R_s = 5'$, $(S/N)_t = 2.9$ for a universal magnitude cut $\text{Mag}_c = -21.5$. For other combinations of magnitude cut, $2.3 \leq (S/N)_t \leq 3.2$. For $R_s = 3'$, $2.7 \leq (S/N)_t \leq 3.2$. Therefore we have achieved a measurement of the ISW effect induced by low-density regions of the universe, at a significance of 3.2σ .

This 3.2σ detection is comparable to the 3.4σ detection directly using galaxies (Table 2). This is an interesting point to address and to further investigate. First, this LDP-ISW cross-correlation is not equivalent to directly using galaxies, since the LDP overdensity δ_l -galaxy overdensity δ_g relation is nonlinear and non-local. For this reason, it is not subject to the $\sim 7\sigma$ upper bound of S/N in galaxy-ISW cross-correlation measurement, for ideal CMB/galaxy surveys (Afshordi 2004). Second, given that the weighting that we adopt to

convert LDPs to δ_l is not optimal, the S/N should further improve if we find and apply the optimal weighting. This is an issue for future investigation.

We caution that the estimated S/N depends on the estimation of covariance matrix and its inversion. We will discuss another estimation of covariance matrix using the Jackknife resampling method, and the inversion of noisy covariance matrix with the SVD method. The results shown in the main text use the covariance matrix estimated by rotating CMB (hereafter *Rot.*), and the inversion by keeping the first two eigenmodes of the covariance matrix. Table 2 shows the S/N of other choices.

Table 2. S/N of $\omega_{T\ell(g)}^o$.

COV	$R_s[\text{arcmin}]_{z_m}$	$\text{Mag}_c - 5\text{lgh}$	S/N				Max(S/N _t)
			-20.5	-21	-21.5	-22	
<i>Rot.</i>	3	0.1	1	1.1	0.9	-	3.2
		0.3	-	1.9	2.2	1.5	
		0.5	-	-	2.1	2.1	
<i>Rot.</i>	5	0.1	1	1.2	0.9	-	3.2
		0.3	-	1.2	2.1	1.4	
		0.5	-	-	1.8	2.1	
<i>Jack.</i>	3	0.1	1.5	1.4	1.2	-	3.7
		0.3	-	2.1	2.5	2	
		0.5	-	-	2.3	2.3	
<i>Jack.</i>	5	0.1	1.4	1.5	1.2	-	3.6
		0.3	-	1.3	2.3	1.8	
		0.5	-	-	1.8	2.3	
<i>Rot.</i>	galaxy	0.1	0.9	1	0.9	-	3.4
		0.3	-	2.4	2.3	1.5	
		0.5	-	-	2.2	2.1	

‘*Rot.*’ represents for using the CMB-rotation technique to estimate the covariance matrix.

‘*Jack.*’ represents for using the Jackknife technique.

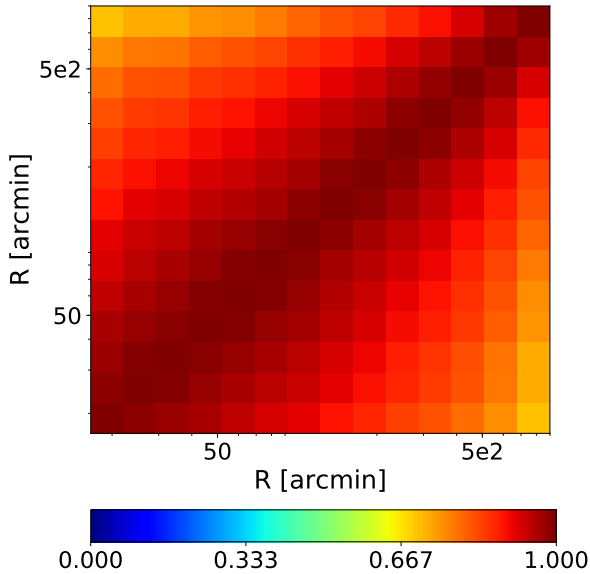
The last three rows are for CMB-galaxy correlation measurement.

Table 3. The bestfit A_{ISW} , the associated $1\text{-}\sigma$ uncertainty, and χ_{min}^2 , combining all three redshifts.

COV	$R_s[\text{arcmin}]$	Max($\text{Mag}_c - 5\text{lgh}$)	$\langle A_{\text{ISW}} \rangle$		χ_{min}^2		
			-21.5	Min($\text{Mag}_c - 5\text{lgh}$)	Max($\text{Mag}_c - 5\text{lgh}$)	-21.5	Min($\text{Mag}_c - 5\text{lgh}$)
<i>Rot.</i>	3.	1.14±0.38	1.18±0.39	1.07±0.42	0.36	0.89	1.1
<i>Rot.</i>	5	0.9±0.4	1.07±0.4	1.06±0.42	0.29	0.79	1
<i>Rot.</i>	galaxy	1.25±0.38	1.21±0.38	1.07±0.42	0.69	1	1.2

For $z_m = 0.1, 0.3, 0.5$, Max($\text{Mag}_c - 5\text{lgh}$) equals to -20.5, -21, -21.5 respectively.

For $z_m = 0.1, 0.3, 0.5$, Min($\text{Mag}_c - 5\text{lgh}$) equals to -21.5, -22, -22 respectively.

**Figure 9.** The covariance matrix for $\omega_{T\ell}^o$. It is calculated with the *Rot.* strategy for parameters $z_m = 0.3$, $\text{Mag}_c - 5\text{lgh} = -21.5$ and $R_s = 5'$. Further discussions and more results are presented in the appendix.

4.3 Comparison with theoretical prediction

Clearly, Fig. 7 & 8 show that the measurements are in good agreement with the prediction of the concordance ΛCDM cosmology. To further quantify the agreement, we choose the model of fitting as

$$\omega_{T\ell}^o = A_{\text{ISW}} \omega_{T\ell}^s. \quad (12)$$

Here A_{ISW} is the amplitude to fit and the standard ΛCDM cosmology has $A_{\text{ISW}} = 1$. We minimize

$$\begin{aligned} \chi^2 &= \delta\omega(\theta_i) C_{ij}^{-1} \delta\omega(\theta_j), \\ \delta\omega(\theta) &\equiv \omega_{T\ell}^o - \omega_{T\ell}^s. \end{aligned} \quad (13)$$

to obtain the bestfit A_{ISW} . The bestfit A_{ISW} and its 1σ uncertainty is shown in Fig. 7 & 8. We find that constrained A_{ISW} of all LDP samples are consistent with unity, within 1σ statistical uncertainty. Therefore the concordance ΛCDM indeed describes the data excellently.

We further combine all three redshifts to constrain A_{ISW} . The constraint depends on which sample is used for each redshift. If using the largest galaxy sample at each redshift, we obtain

$$\begin{aligned} A_{\text{ISW}}(R_s = 3') &= 1.14 \pm 0.38, \\ A_{\text{ISW}}(R_s = 5') &= 0.9 \pm 0.4. \end{aligned} \quad (14)$$

In Table 3 we show A_{ISW} estimated from various combinations, all consistent with unity. It also shows the minimum chi-square χ_{min}^2 corresponding to are all smaller than 1.2, demonstrating excellent agreement with ΛCDM . In contrast

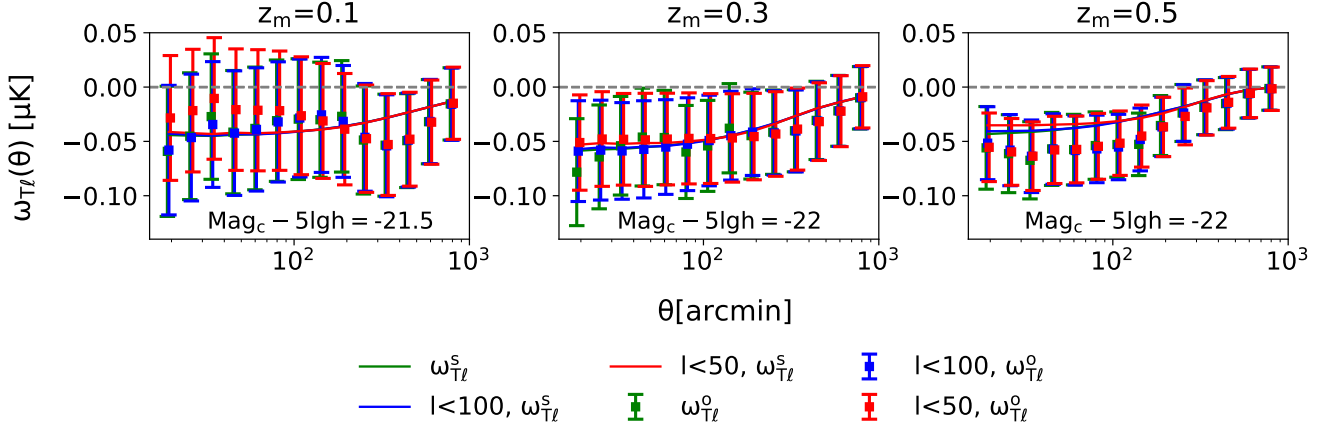


Figure 10. Testing the origin of the detected cross-correlation, by a tophat cut in multipole ℓ space ($\ell_{\text{cut}} = 50, 100$, and no cut). The cut $\ell_{\text{cut}} = 100$ has essentially no impact on $\omega_{T\ell}$, showing that the cross-correlation signal mainly arises from $\ell < 100$. In contrast, the cut $\ell_{\text{cut}} = 50$ causes visible difference in $\omega_{T\ell}$, showing that contribution from $50 < \ell < 100$ is non-negligible. These dependences are consistent with the ISW origin.

to previous constraints of $A_{\text{ISW}} \gg 1$ (Hunt & Sarkar 2010; Inoue et al. 2010; Nadathur et al. 2012; Ilić et al. 2014; Cai et al. 2014; Hotchkiss et al. 2015; Kovács & Granett 2015; Kovács et al. 2017; Kovács 2018; Kovács et al. 2019), we find no tension with the concordance Λ CDM. Furthermore, this agreement holds for different thresholds of R_s (and therefore under-density).

4.4 Further consistency checks

The detected signal arises from the low-density regions of the universe, but free of many selection effects of void identification. Nevertheless, given the known difficulties in ISW measurements, we carry out three more tests in order to further validate the measurements.

- First is to check the origin of the cross-correlation. The ISW effect is expected to arise from large scale and is insensitive to small scale CMB modes. Fig. 10 shows the measured LDP-CMB cross correlation with a tophat cut $\ell_{\text{cut}} = 50, 100$ in multipole ℓ space. We find that the results with $\ell_{\text{cut}} = 100$ are almost identical to the ones without a cut. Therefore the measured cross-correlation indeed comes from the large angular scale, as expected. Furthermore, the cut $\ell_{\text{cut}} = 50$ results in minor but visible loss of the cross correlation signal, in particular for the lowest redshift bin $0.01 < z < 0.2$. This is again expected if the signal arises from the ISW effect. The k corresponding to a given ℓ is roughly $k \sim \ell/r(z)$. For the same ℓ , lower redshift means larger scale (smaller k) and therefore larger loss of signal.

- We also check the measured galaxy density-ISW cross correlation, using the same galaxy samples and the same analysis pipeline. The overall S/N reaches 3.4 (Table 2). And the results are also in good agreement with the Λ CDM prediction, $A_{\text{ISW}} = 1.21 \pm 0.38$ for $\text{Mag}_c - 5\text{lgh} = -21.5$. Since the galaxy overdensity field and the LDP overdensity field are defined very differently, both agreements with Λ CDM further validate our measurements.

- Besides the Planck SMICA map, we have other CMB maps to analyze. We have tried the Planck 100 GHz map and the V-band WMAP map. After subtracting the foregrounds, the results are consistent.

Therefore we believe the robustness of our LDP-ISW detection. The excellent consistency with Λ CDM then implies hidden systematics in some of the void-ISW cross correlation measurements. Therefore this LDP method is highly complementary to existing methods to cross-check and improve the ISW measurement.

5 SUMMARY & DISCUSSION

We have designed a novel method of ISW measurement, by cross-correlating LDPs (low-density-positions, Dong et al. (2019)) and CMB. We then apply it to the DESI imaging survey DR8 galaxy catalogue of BASS + MZLS + DeCALs + DES, and Planck SMICA map. We achieve a 3.2σ detection of the ISW effect (Table 2), one of the most significant among existing measurements. Furthermore, the detected signal is fully consistent with the concordance Λ CDM prediction ($A_{\text{ISW}} = 1$) for all the galaxy samples that we investigated and the adopted LDP definitions (Table 3), with the bestfit A_{ISW} consistent with $A_{\text{ISW}} = 1$ and $\chi^2 \in (0.3, 1.1)$. For example, for $\text{Mag}_c - 5\text{lgh} = -21.5$ and $R_s = 3'$, we find $A_{\text{ISW}} = 1.18 \pm 0.39$, with $\chi^2_{\text{min}} = 0.89$. For $R_s = 5'$, $A_{\text{ISW}} = 1.07 \pm 0.4$ and $\chi^2_{\text{min}} = 0.79$.

The achieved S/N (3.2σ) is already competitive to that with galaxy-ISW cross correlation (3.4σ that we have measured), and there exists room for further improvement. Together with the excellent agreement with the concordance cosmology, we have demonstrated the applicability of the LDP method to measure the ISW effect, for the first time. Our measurement provides an independent check to existing tensions between void ISW and Λ CDM, and between void ISW and galaxy ISW. Since our LDP ISW measurement has

no tension with Λ CDM prediction and galaxy ISW measurement, we suggest hidden systematics in void ISW measurements.

The measurement can be used to constrain dark energy, in particular given a flat geometry. There are potentially other applications. For example, galaxy overdensity and LDP overdensity probe regions of the universe with statistically different matter density/gravitational potential. So the combination of LDP ISW and galaxy ISW may probe beyond Λ CDM physics, such as clustered dark energy and screening phenomena in modified gravity models.

Although the measurement S/N is already high among existing ISW detections, there are still possible improvements, related to the LDP definition and the LDP overdensity definition.

- LDP definition. LDPs depend on the galaxy sample, which is in turn determined by the redshift range and radius threshold, magnitude cut, and other galaxy properties. We have only tried a few configurations and the obtained S/N is unlikely optimal.

- LDP overdensity δ_1 definition. The underlying matter density δ_m at LDPs is statistically negative. But the exact value varies with LDPs. For example, δ_m at LDPs surrounded by LDPs should be on average more negative than LDPs surrounded by non-LDPs. Intuitively speaking, δ_m should decrease monotonically with increasing d_{\min} , the distance of a given LDP to the nearest galaxy. The overdensity definition (Eq. 2) reflects this expectation. It is indeed tightly (negatively) correlated with the underlying matter density field, as verified with our simulation (Fig. 5). However, although it has enabled a 3.2σ detection of the ISW effect, it is still an open question on whether it is the optimal choice. For example, for the adopted definition of δ_1 , its value equals to $\text{Max}(\delta_1)$ in void regions of size $\gg 6.87'$. So it downweights the contribution from large voids. The optimal δ_1 definition must take it into account. From the viewpoint of ISW measurement, the optimal definition of δ_1 should result in a cross-correlation coefficient with the gravitational potential field as close to unity as possible.

- The way to populate galaxies. In this work we use the SHAM method to populate galaxies in simulation by allowing a scatter σ_{Mag} between galaxy luminosity and halo/subhalo mass and a scatter σ_z between the true galaxy redshift and photometrical redshift. Adding σ_{Mag} will decrease the nominal absolute magnitude on average, as more fainter galaxies are mistaken for bright ones statistically. While adding σ_z will increase the nominal absolute magnitude on average, as more brighter galaxies at higher redshifts are mistaken as fainter galaxies at lower redshifts. So these two uncertainties would lead to the so-called Eddington bias (Eddington 1913). For example, when $z_m = 0.3$ and $\text{Mag}_c - 5\text{lgh} = -21$, the number of galaxies increases by 5%, while the galaxy sample becomes 1.2 times larger for $\text{Mag}_c - 5\text{lgh} = -22$. Our solution is to redo the SHAM after introducing these uncertainties. Otherwise, the distribution of galaxies with magnitude is changed. Although this is still a rough model to populate galaxies, the comparison of correlation-function in Fig.4 show the rationality of our operation.

- The estimator of cross correlation function. We adopt a simple cross correlation function estimator. More opti-

mal estimator requires input of galaxy selection function. DESI imaging survey galaxy catalogue still contains various imaging systematics, not fully captured by the random catalogue that we use (Kitanidis et al. 2020). The resulting non-uniform selection function biases the galaxy auto correlation measurement. The problem for the cross correlation that we perform in this paper is much less severe, since the galaxy selection function is uncorrelated with CMB and ISW. Furthermore, to a good approximation, it is uncorrelated to residual foreground in the Planck CMB map. Nevertheless, non-uniform galaxy selection function amplifies statistical error in the cross correlation measurement. Future work needs to suppress such error (and diagnose potential systematics) by improving the cross correlation estimator with the aid of random catalogue.

Besides these measurement issues, accurate determination of the covariance matrix and robust estimation of the S/N and A_{ISW} is also important. In the appendix, we have presented our treatments on the covariance matrix and its inverse. We plan to further investigate these issues, with the aid of numerical simulations and mock catalogues.

There are other possibilities to further explore. In principle the cross-correlation in real space is identical to that in Fourier (spherical harmonic) space. But in reality, due to the scale cut, mask and noise/foreground distribution, the two can differ. In this paper we only work on the real space, and leave the analysis in Fourier space elsewhere. For the theory/simulation side, we have used SHAM to populate galaxies into N-body simulation. This exercise turns out to be successful. Nevertheless, there may still room of improvement for higher S/N and better theoretical prediction.

ACKNOWLEDGEMENTS

We thank Yipeng Jing for providing us the N-body simulation. We also thank Jian Yao and Ji Yao for useful discussions. This work is supported by the National Key Basic Research and Development Program of China (No.15ZR1446700, 2018YFA0404504,19ZR1466800), the NSFC grants (11621303,11653003,11673016,11833005,11890692,11773048), the 111 project (No. B20019).

REFERENCES

- Abbott T. M. C., et al., 2018, *ApJS*, **239**, 18
 Afshordi N., 2004, *Phys. Rev. D*, **70**, 083536
 Afshordi N., Loh Y.-S., Strauss M. A., 2004, *Phys. Rev. D*, **69**, 083524
 Ansarinejad B., Mackenzie R., Shanks T., Metcalfe N., 2019, arXiv e-prints, p. arXiv:1909.11095
 Bean R., Doré O., 2004, *Phys. Rev. D*, **69**, 083503
 Blum R. D., et al., 2016, in American Astronomical Society Meeting Abstracts #228. p. 317.01
 Boughn S., Crittenden R., 2004, *Nature*, **427**, 45
 Boughn S. P., Crittenden R. G., 2005, *New Astron. Rev.*, **49**, 75
 Cabré A., Fosalba P., Gaztañaga E., Manera M., 2007, *MNRAS*, **381**, 1347
 Cabré A., Gaztañaga E., Manera M., Fosalba P., Castander F., 2006, *Monthly Notices of the Royal Astronomical Society: Letters*, **372**, L23

Cai Y.-C., Cole S., Jenkins A., Frenk C. S., 2010, *MNRAS*, **407**, 201

Cai Y.-C., Neyrinck M. C., Szapudi I., Cole S., Frenk C. S., 2014, *ApJ*, **786**, 110

Corasaniti P.-S., Giannantonio T., Melchiorri A., 2005, *Phys. Rev. D*, **71**, 123521

Crittenden R. G., Turok N., 1996, *Phys. Rev. Lett.*, **76**, 575

DESI Collaboration et al., 2016, arXiv e-prints, p. arXiv:1611.00036

Dong F., et al., 2019, *ApJ*, **874**, 7

Eddington A. S., 1913, *MNRAS*, **73**, 359

Fang W., Hu W., Lewis A., 2008, *Phys. Rev. D*, **78**, 087303

Fosalba P., Gaztañaga E., 2004, *MNRAS*, **350**, L37

Fosalba P., Gaztañaga E., Castander F. J., 2003, *ApJ*, **597**, L89

Giannantonio T., et al., 2006, *Phys. Rev. D*, **74**, 063520

Giannantonio T., Crittenden R., Nichol R., Ross A. J., 2012, *MNRAS*, **426**, 2581

Górski K. M., Hivon E., Banday A. J., Wandelt B. D., Hansen F. K., Reinecke M., Bartelmann M., 2005, *ApJ*, **622**, 759

Granett B. R., Neyrinck M. C., Szapudi I., 2008, *ApJ*, **683**, L99

Han J., Frenk C. S., Eke V. R., Gao L., White S. D. M., Boyarsky A., Malyshev D., Ruchayskiy O., 2012, *MNRAS*, **427**, 1651

Hernández-Monteagudo C., 2010, *A&A*, **520**, A101

Hernández-Monteagudo C., et al., 2014, *MNRAS*, **438**, 1724

Hinshaw G., et al., 2013, *ApJS*, **208**, 19

Hotchkiss S., Nadathur S., Gottlöber S., Iliev I. T., Knebe A., Watson W. A., Yepes G., 2015, *MNRAS*, **446**, 1321

Hu W., 2003, *Annals of Physics*, **303**, 203

Hu W., Scranton R., 2004, *Phys. Rev. D*, **70**, 123002

Hunt P., Sarkar S., 2010, *MNRAS*, **401**, 547

Ilić S., Langer M., Douspis M., 2014, *A&A*, **572**, C2

Inoue K. T., Sakai N., Tomita K., 2010, *ApJ*, **724**, 12

Jarvis M., 2015, TreeCorr: Two-point correlation functions (ascl:1508.007)

Jing Y., 2019, *Science China Physics, Mechanics, and Astronomy*, **62**, 19511

Khosravi S., Mollazadeh A., Baghran S., 2016, *J. Cosmology Astropart. Phys.*, **2016**, 003

Kitanidis E., et al., 2020, *MNRAS*,

Kovács A., 2018, *MNRAS*, **475**, 1777

Kovács A., Granett B. R., 2015, *MNRAS*, **452**, 1295

Kovács A., et al., 2017, *MNRAS*, **465**, 4166

Kovács A., et al., 2019, *MNRAS*, **484**, 5267

López-Corredoira M., Sylos Labini F., Betancort-Rijo J., 2010, *A&A*, **513**, A3

Massardi M., Bonaldi A., Negrello M., Ricciardi S., Raccanelli A., de Zotti G., 2010, *MNRAS*, **404**, 532

McEwen J. D., Vielva P., Hobson M. P., Martínez-González E., Lasenby A. N., 2006, arXiv e-prints, pp astro-ph/0602398

Mota D. F., Shaw D. J., Silk J., 2008, *ApJ*, **675**, 29

Nadathur S., Hotchkiss S., Sarkar S., 2012, *J. Cosmology Astropart. Phys.*, **2012**, 042

Nolta M. R., et al., 2004, *ApJ*, **608**, 10

Padmanabhan N., Hirata C. M., Seljak U., Schlegel D. J., Brinkmann J., Schneider D. P., 2005, *Phys. Rev. D*, **72**, 043525

Pápai P., Szapudi I., Granett B. R., 2011, *ApJ*, **732**, 27

Planck Collaboration et al., 2014, *A&A*, **571**, A19

Planck Collaboration et al., 2016a, *A&A*, **594**, A13

Planck Collaboration et al., 2016b, *A&A*, **594**, A21

Raccanelli A., Bonaldi A., Negrello M., Matarrese S., Tormen G., de Zotti G., 2008, *MNRAS*, **386**, 2161

Rác G., Dobos L., Beck R., Szapudi I., Csabai I., 2017, *MNRAS*, **469**, L1

Rassat A., Land K., Lahav O., Abdalla F. B., 2007, *MNRAS*, **377**, 1085

Sachs R. K., Wolfe A. M., 1967, *ApJ*, **147**, 73

Sawangwit U., Shanks T., Cannon R. D., Croom S. M., Ross N. P.,

Wake D. A., 2010, *Monthly Notices of the Royal Astronomical Society*, **402**, 2228

Schiavon F., Finelli F., Gruppuso A., Marcos-Caballero A., Vielva P., Crittenden R. G., Barreiro R. B., Martínez-González E., 2012, *MNRAS*, **427**, 3044

Seljak U., Zaldarriaga M., 2000, *ApJ*, **538**, 57

Shajib A. J., Wright E. L., 2016, *The Astrophysical Journal*, **827**, 116

Silva D. R., et al., 2016, in American Astronomical Society Meeting Abstracts #228. p. 317.02

The Dark Energy Survey Collaboration 2005, arXiv e-prints, pp astro-ph/0510346

Vielva P., Martínez-González E., Tucci M., 2006, *MNRAS*, **365**, 891

Weller J., Lewis A. M., 2003, *MNRAS*, **346**, 987

Wright E. L., et al., 2010, *AJ*, **140**, 1868

Yang X., Mo H. J., van den Bosch F. C., 2008, *ApJ*, **676**, 248

Zhang P., 2006, *Phys. Rev. D*, **73**, 123504

Zou H., et al., 2019, *ApJS*, **245**, 4

de Putter R., Huterer D., Linder E. V., 2010, *Phys. Rev. D*, **81**, 103513

APPENDIX A: PERFORMING SINGULAR-VALUE DECOMPOSITION TO COVARIANCE MATRIX

In §4.2 we find that S/N of the observational signal $\omega_{T\ell}^o$ is overestimated compared to the one calculated with the theoretical line $\omega_{T\ell}^s$, using the same covariance matrix. Here we perform the Singular-Value Decomposition (SVD) on C_{ij} for further analysis:

$$\mathbf{C} = \mathbf{U}\mathbf{\Lambda}\mathbf{U}^T. \quad (\text{A1})$$

Since the covariance matrix \mathbf{C} is symmetric and real, all the eigenvalues λ_i are real. Since it is positive definite, all $\lambda_i > 0$. $\mathbf{\Lambda} = \text{diag}(\lambda_i)$, and λ_i is the i -th eigenvalue ($\lambda_1 \geq \lambda_2 \dots$). \mathbf{U} is a rotation orthogonal matrix ($\mathbf{U}^T\mathbf{U} = \mathbf{I}$), with the i -th eigenvectors of \mathbf{C} as its i -th column vectors. Noise in \mathbf{C} contaminates these eigenvectors. The ones with smaller eigenvalues have larger errors, which are further amplified in \mathbf{C}^{-1} . Together with noise in ω , this causes error in the estimated S/N. The SVD (or pseudo-inverse) then modifies \mathbf{C}^{-1} to

$$\mathbf{C} = \mathbf{U} \text{diag}(\lambda_1^{-1}, \lambda_2^{-1}, \dots, \lambda_M^{-1}, \mathbf{0}, \dots) \mathbf{U}^T. \quad (\text{A2})$$

Namely, it disregards the $i > M$ eigenvectors in the inverse of $\tilde{\omega}$ to stabilize the inverse and to reduce the impact of noise in \mathbf{C} . The task now is to determine M .

\mathbf{C} in our case is a $N \times N$ ($N = 14$) matrix. The one shown in Fig.9 has $\lambda_i = 12.74, 0.82, 0.21, 0.09, 0.05, 0.02, \dots$. We have checked that the first 2-3 eigenmodes captures major features of \mathbf{C} . But the other eigenmodes cause large variation in \mathbf{C}^{-1} and S/N, due to the $1/\lambda$ operation in \mathbf{C}^{-1} . We perform two convergence tests to determine M .

- Fig.1 shows the S/N of $\omega_{T\ell}^{o(s)}$ as a function of M . S/N of $\omega_{T\ell}^o$ is sensitive to the $M > 2$ eigenmodes, despite the fact that these eigenmodes has insignificant contribution to \mathbf{C} . In contrast, the S/N of $\omega_{T\ell}^s$ becomes very stable in all cases when $M \geq 2$. These results suggest $M = 2, 3$ as a reasonable choice of SVD and S/N estimation.

- We also test the stability of S/N against artificial bump ($\sigma_\omega^o/3$) added to $\omega_{T\ell}^s$, each at a single θ (Fig.A1). Since the

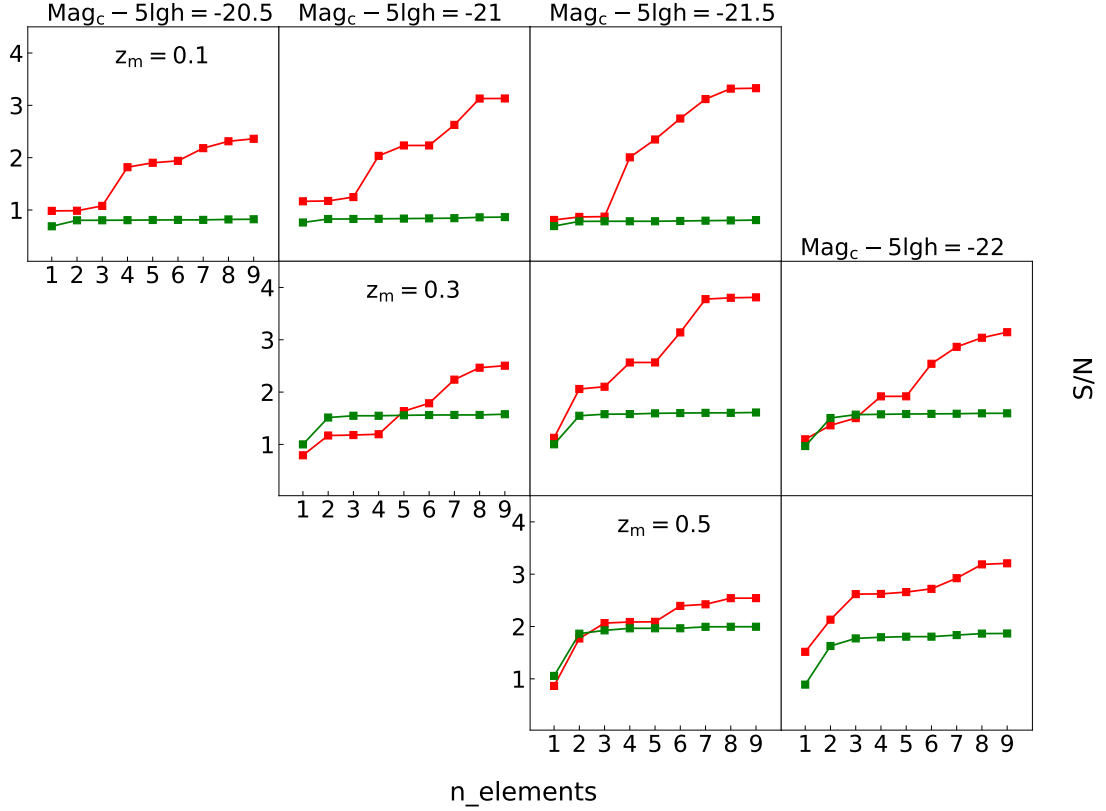


Figure 1. The estimated S/N by keeping the first n_{elements} eigenmodes in the SVD procedure. The red line is for $\omega_{T\ell}^o$, and the green line is for $\omega_{T\ell}^s$. The critical radius R_s equals to $5'$. This tests suggest to keep the first 2-3 eigenmodes.

added bump is only 1/3 of the statistical scatter, we expect insignificant change in S/N, otherwise something in \mathbf{C}^{-1} may be wrong. We find that for $M = 2, 3$ the S/N is indeed stable.

Therefore $M = 2, 3$ are reasonable choices for our situation. $M = 3$ leads to a larger S/N. To be conservative, we adopt $M = 2$ to estimate the S/N.

APPENDIX B: JACK-KNIFE RESAMPLING

In this section, we estimate error bars using the jackknife resampling technique by dividing the whole sky into fields at a resolution of $N_{\text{side}} = 4$ (resolution equals to 879 arcmin). If the number of LDPs within a field is too few either due to the mask effect or the edge effect, we will merge it into one of its neighboring field, whose number of LDPs is the fewest. In this way, the number distribution of LDPs in different fields become more homogeneous. The CMB pixels are also divided into the same fields. Jack-knife subsamples are then generated by removing one field at onetime, with C_{ij} given

as:

$$C_{ij} = \frac{N_J - 1}{N_J} \sum_{n=1}^{N_J} [(\omega_{T\ell,n}^J(\theta_i) - \overline{\omega_{T\ell,n}^J(\theta_i)}) \times (\omega_{T\ell,n}^J(\theta_j) - \overline{\omega_{T\ell,n}^J(\theta_j)})], \quad (\text{B1})$$

where $\omega_{T\ell,n}^J$ is the cross-correlation measured for the n -th subsample, $\overline{\omega_{T\ell,n}^J}$ is the average of subsamples' measurements, and i and j refer to the i -th and j -th radial bins.

With these covariance matrices, we recalculate S/N. As shown in Table 2, they are found 10%-20% higher than those estimated with *Rot.* technique, since smaller error bars and lower off-diagonal terms of C_{ij} are found with jack-knife resampling technique. One possible explanation is that jack-knife error would underestimate ISW errors, as pointed out in Padmanabhan et al. (2005). To be conservative, we do not adopt these higher S/N.

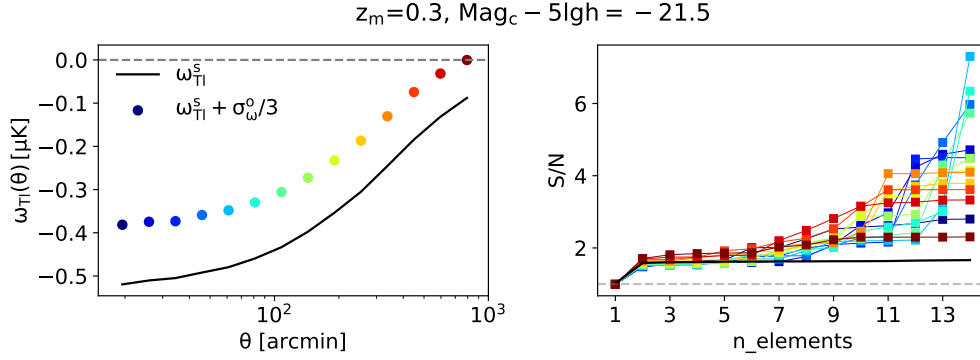


Figure A1. The stability of S/N (right panel) against a small bump artificially added to $\omega_{\text{Tl}}^{\text{s}}$ (left panel). This test rules out the possibility of keeping the eigenmodes $i \geq 5$, and supports the option of keeping the first 2-3 eigenmodes.

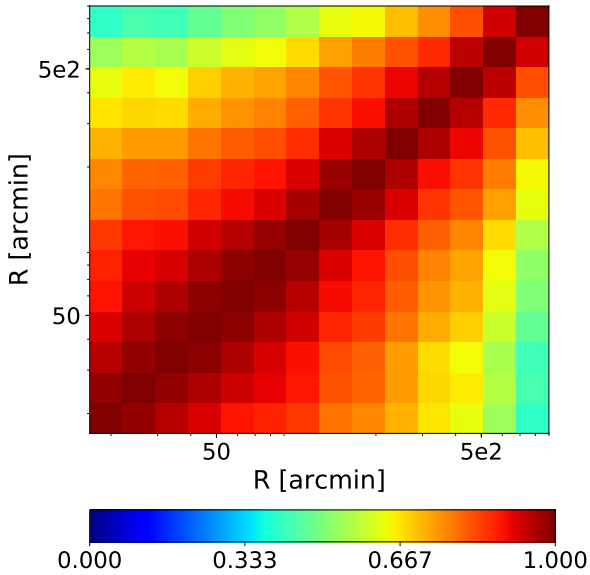


Figure B1. Similar to Fig.9, but estimated using the jackknife resampling technique.

APPENDIX C: ISW SIGNAL MEASURED WITH GALAXIES

Although the findings of ISW effect detected with galaxies seem to be conclusive, situation is more complicated. In [Sawangwit et al. \(2010\)](#), negative signals are measured for $z = 0.7$ with luminous red galaxy (LRG) sample, while good consistent is found between data and the standard ISW model for lower redshifts. This conclusion is further confirmed by [Ansarinejad et al. \(2019\)](#) with larger galaxy sample. In [Khosravi et al. \(2016\)](#), ISW-LRG signals have been found to be higher than Λ CDM, and an evolved halo bias has to be introduced to solve the discrepancy. In [López-Corredoira et al. \(2010\)](#), the author concludes that there is no evidence yet of a significant detection of the integrated Sachs-Wolfe (ISW) effect after repeating the analyses in some papers, since field-to-field fluctuations are found to

dominate the detected signals. Much of the uncertainty in these studies arises from the Poisson noise in the galaxy distribution. So one of the key to further verify these problems is to increase the survey area to decrease the statistical errors.

Considering that the current sky coverage of DESI DR8 galaxy catalog approaches 20000 deg², in this section we revisit the CMB-galaxy correlation. The results are shown in Fig.C1, in which the grouping of galaxies is same to Fig.7. The error bars are estimated using *Rot.* technique. One can find that these signals are close in amplitudes, $\sim 0.5 \mu\text{K}$ for $\theta < 50'$, although they corresponds to different galaxy samples. In general, they are consistent with the prediction curves from simulation. The A_{ISW} measured in each panel is close to 1.

This paper has been typeset from a $\text{\TeX}/\text{\LaTeX}$ file prepared by the author.

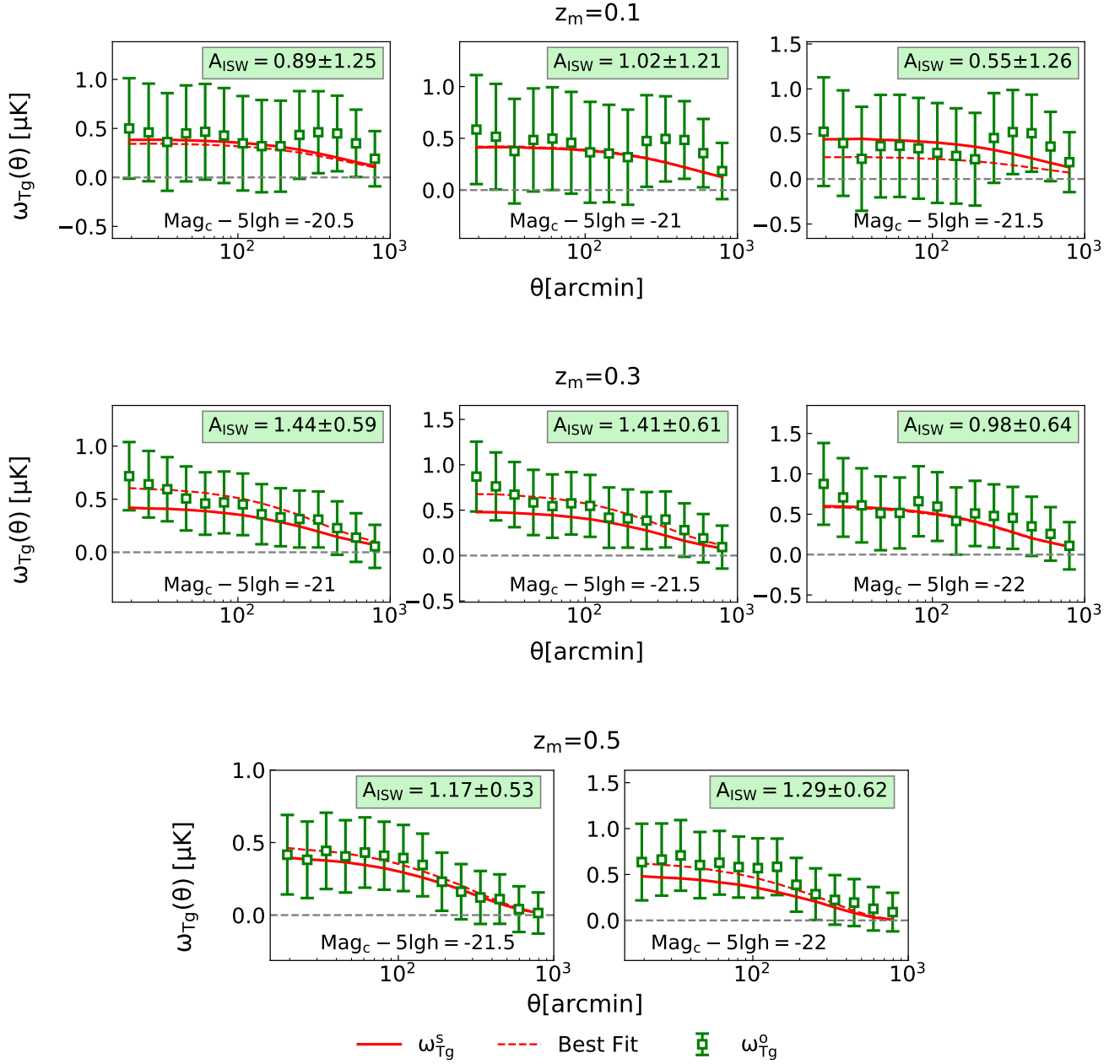


Figure C1. The cross-correlation between galaxies and temperature fluctuations. The panels are arranged in a similar way with Fig.7.